AIAA JOURNAL
Vol. 42, No. 5, May 2004

# Performance of Upwind Schemes and Turbulence Models in Hypersonic Flows

Turan Coratekin,* Jörn van Keuk,† and Josef Ballmann‡
*Rheinisch–Westfälische Technische Hochschule Aachen, D-52062 Aachen, Germany*

**An evaluation of three upwind schemes and four turbulence models is presented in order to assess their respective separate and combined performance in complex hypersonic flows with large scale separation. The upwind schemes include Liou and Steffen's advection upstream splitting method (AUSM) flux-vector splitting, its modification by Wada and Liou, called AUSMDV, and Roe's flux-difference splitting. Turbulent effects were modeled utilizing Wilcox's $k$–$\omega$ model with two compressibility corrections by Coakley's group, the widely popular Spalart–Allmaras and supersonic transport (SST) models as well as an explicit algebraic Reynolds stress model (EARSM) by Wallin and Johansson. Using a powerful explicit/implicit finite volume computational-fluid-dynamics code, the upwind schemes are first tested on a complex double-wedge Euler flow configuration. A three-dimensional corner flow serves as a test case for a laminar Navier–Stokes computation. Finally, AUSM schemes are used in combination with several turbulence models in a two-dimensional ramp flow and a three-dimensional crossing-shock interaction. Results are compared with either experiments or computations by other authors. The authors' conclusions suggest that the AUSMDV is probably the most recommendable scheme for complex hypersonic flows. Regarding turbulence modeling, models with explicit compressibility corrections, in this case the $k$–$\omega$ model, seem to deliver presently the comparatively best predictions in complex flows, particularly in case of separation.**

## Nomenclature

| | | |
|---|---|---|
| $a$ | = | speed of sound |
| $\boldsymbol{a}$ | = | Reynolds-stress anisotropy tensor |
| $C_{D\omega}$ | = | coefficient in $\omega$ production term |
| $C_F$ | = | skin friction |
| $c_v$, $c_p$ | = | specific heats at constant volume/pressure |
| $D_\omega$ | = | production term in $\omega$ equation |
| $e$ | = | specific total energy |
| $\boldsymbol{F}$, $\boldsymbol{G}$, $\boldsymbol{H}$ | = | fluxes |
| $\hat{\boldsymbol{F}}$, $\hat{\boldsymbol{G}}$, $\hat{\boldsymbol{H}}$ | = | discretized fluxes |
| $H_t$ | = | specific total enthalpy |
| $\boldsymbol{I}$ | = | unit tensor, components $\delta_{ij}$ |
| $II_S$, $II_W$ | = | invariants in the explicit algebraic Reynolds stress model (EARSM) |
| $IV$, $V$ | = | invariants in the EARSM |
| $k$ | = | specific turbulence kinetic energy |
| $l$ | = | turbulent length scale |
| $M$ | = | Mach number |
| $n$ | = | index in compressibility correction |
| $p$ | = | pressure |
| $\boldsymbol{Q}$ | = | source term vector |
| $q_i$ | = | component of the heat-flux vector |
| $R$ | = | perfect-gas constant |
| $Re_s$ | = | Reynolds number based on length $s$ |
| $\boldsymbol{Res}$ | = | residual |
| $\boldsymbol{S}$ | = | normalized mean strain-rate, tensor |
| $s$ | = | switch function in AUSMDV scheme |
| $T$ | = | temperature |
| $t$ | = | time |
| $t_{ij}$ | = | component of molecular stress tensor |
| $\boldsymbol{U}$ | = | vector of conservative variables |
| $u$, $v$, $w$ | = | components of velocity vector |
| $V$ | = | volume |
| $\boldsymbol{W}$ | = | rotation tensor |
| $x$, $y$, $z$ | = | Cartesian coordinates |
| $y$ | = | wall distance |
| $\alpha$, $\alpha^*$ | = | turbulence model coefficients |
| $\alpha_k$ | = | strength of $k$th wave in Riemann problem |
| $\beta_{i=1,\ldots,10}$ | = | EARSM coefficients |
| $\beta$, $\beta^*$ | = | turbulence model coefficients |
| $\delta$ | = | small change, boundary-layer thickness, entropy fix parameter |
| $\epsilon$ | = | turbulent dissipation per unit mass |
| $\lambda_k$ | = | $k$th wave propagation speed in Riemann problem |
| $\mu_{\text{mol}}$ | = | molecular viscosity |
| $\mu_T$ | = | eddy viscosity |
| $\rho$ | = | density |
| $\sigma$, $\sigma^*$ | = | coefficients in turbulence model |
| $\tau_{ij}$ | = | component of Reynolds-stress tensor |
| $\omega$ | = | specific turbulent dissipation rate |

*Subscripts*

| | | |
|---|---|---|
| $i$, $j$, $k$ | = | cartesian coordinate direction |
| $l$, $m$, $n$ | = | mesh point locations |
| $w$, wall | = | wall, surface data |
| $\xi$, $\eta$, $\zeta$ | = | dimensionless difference variables in local coordinates |
| $\infty$ | = | freestream |

*Superscripts*

| | | |
|---|---|---|
| $c$ | = | convective term |
| $v$ | = | viscous term |
| $+$, $-$ | = | split quantities in advection upstream splitting method (AUSM) scheme |
| - | = | Reynolds-averaged quantity |
| ~ | = | Favre-averaged quantity |
| $'$ | = | Reynolds fluctuation |
| $''$ | = | Favre fluctuation |

Received 12 April 2001; accepted for publication 5 October 2003. 

*Research Assistant, DFG Graduiertenkolleg 5/3 "Transport Phenomena in Hypersonic Flows," Lehr- und Forschungsgebiet für Mechanik.

†Research Assistant, DFG Collaborative Research Center SFB 253 "Fundamentals of Design of Aerospace Planes," Lehr- und Forschungsgebiet für Mechanik.

‡Professor and Director of Lehr- und Forschungsgebiet für Mechanik. Member AIAA.

## Introduction

HYPERSONIC flow became a popular research area about 50 years ago when the military and aerospace industries

recognized the importance of the field for their respective interests. Future aerospace planes, for example, will probably operate within a wide range of Mach numbers ($0.2 \leq M_\infty \leq 9.0$), at altitudes up to 35 km and Reynolds numbers around $10^8$. The emergence of computational fluid dynamics (CFD) certainly was one of the key factors in the success of many past space programs. To ensure a lasting development and a successful future for the aerospace industry, researchers and scientists ought to provide design engineers with the best possible CFD tools. Two distinct research fields have lately gained such tremendous importance within the CFD community that they can be characterized today as the two pacing items in CFD. One of them is the development of upwind schemes, which focuses more essentially on the mathematical point of view, and the other is turbulence modeling. The latter is maybe one of the most complex and unsolved issues of classical physics, and its importance reaches far beyond the special field of hypersonics.

The present paper will test and evaluate three different upwind schemes that have received significant attention within the last years. Liou and Steffen's[1] advection upstream splitting method (AUSM) scheme is a very robust and CPU-efficient scheme belonging to the flux-vector splitting (FVS) group. It is well known for being one of the least dissipative schemes available. A most promising modification to the AUSM scheme was introduced by Wada and Liou.[2] Their AUSMDV scheme improves some of the original AUSM's weaknesses and is even more robust. Still, the AUSMDV's numerical viscosity remains low. Finally, Roe's[3] method is presented as an example of flux-difference splitting (FDS) that explicitly takes into account effects of wave propagation.

Because of the high Reynolds numbers involved in hypersonics, flows are very likely to be fully turbulent. Thus, turbulent effects have to be accounted for, and the most common way to do so is to use the Reynolds-averaging approach. Four turbulence models will be assessed in various hypersonic flow configurations in the following. These include Wilcox's[4] $k$–$\omega$ model in its low-Reynolds-number version, the widely popular Spalart–Allmaras[5] model, Menter's[6] supersonic transport (SST) model, and an explicit algebraic Reynolds-stress model by Wallin and Johansson.[7] Additionally, two compressibility corrections by Coakley and Huang[8] for the $k$–$\omega$ model are reviewed.

The initial step of this investigation will be to test all three upwind schemes in an Euler computation, in order to suppress the influence of viscous effects. It consists first of a two-dimensional double-wedge flow at Mach 9. The complex shock/shock interactions occuring therein are an interesting challenge for any numerical scheme. Complexity is then further increased by considering a three-dimensional laminar Navier–Stokes corner flow at Mach 12. The shock waves interact not only with each other but also with the two boundary layers that appear on each wall. Finally, in an attempt to combine both upwind schemes and turbulence models, two well-known examples for turbulent shock/boundary-layer interactions are presented and investigated. The first one consists in a two-dimensional compression corner flow at Mach 9. The second one is known as a crossing-shock interaction. Here, the incoming turbulent boundary layer at Mach 8 is deflected by two symmetrical fins, which generate two shock waves inside the channel. All results are compared with either experiments or computations by other authors.

The goals of this paper are twofold. First, it shall be investigated how the three upwind schemes perform under hypersonic flow conditions. Recommendations will be made on which schemes are particularly suitable. Second, the turbulence models will be assessed regarding their capability to predict surface data (mainly pressure and heat transfer) in high-speed compressible flows involving large separation regions.

## Physical Model

Continuum mechanics provides the basis for describing unsteady turbulent hypersonic flows of compressible viscous fluids. The corresponding balance equations are the Favre-averaged Navier–Stokes equations with Fourier's law for heat transfer. Additional equations are necessary for the Reynolds stresses, the turbulent dissipation, and other velocity and temperature correlations.

### Governing Equations

All balance equations are used in their integral form but will hereafter be presented in differential form for the sake of brevity. Conservation of mass, momentum, and energy then take the form

$$\frac{\partial(\bar{\rho})}{\partial t} + \frac{\partial(\bar{\rho}\tilde{v}_i)}{\partial x_i} = 0 \tag{1}$$

$$\frac{\partial(\bar{\rho}\tilde{v}_j)}{\partial t} + \frac{\partial(\bar{\rho}\tilde{v}_j\tilde{v}_i)}{\partial x_i} = -\frac{\partial(\bar{p})}{\partial x_j} + \frac{\partial}{\partial x_i}(\bar{t}_{ji} - \overline{\rho v_j'' v_i''}) \tag{2}$$

$$\frac{\partial(\bar{\rho}\tilde{e})}{\partial t} + \frac{\partial}{\partial x_i}[\tilde{v}_i(\bar{\rho}\tilde{e} + \bar{p})] = +\frac{\partial}{\partial x_i}\left(-\bar{q}_i - c_p\overline{\rho v_i'' T''} - \frac{1}{2}\overline{\rho v_j'' v_j'' v_i''}\right)$$
$$+ \frac{\partial}{\partial x_i}(\tilde{v}_j\bar{t}_{ji} + \overline{v_j'' t_{ji}} - \tilde{v}_j\overline{\rho_j'' v_i''}) \tag{3}$$

where Einstein summation convention is applied to repetitive indices.

Presently, air is modeled as a fluid obeying to the perfect-gas equation of state and the perfect-gas caloric equation, which yields the following expressions for the mean pressure $\bar{p}$ and the mass-averaged specific total energy $\tilde{e}$:

$$\bar{p} = \bar{\rho}R\tilde{T}, \qquad \tilde{e} = c_v\tilde{T} + \tfrac{1}{2}\tilde{v}_i\tilde{v}_i + k$$

where $k$ is the mass-averaged turbulence kinetic energy:

$$k = \tfrac{1}{2}(\overline{\rho v_i'' v_i''}/\bar{\rho}) \tag{4}$$

Assuming that the pressure viscosity can be neglected, the mean molecular viscous stress for a Newtonian fluid becomes

$$\bar{t}_{ij} = -\frac{2}{3}\tilde{\mu}_{\text{mol}}\frac{\partial\tilde{v}_k}{\partial x_k}\delta_{ij} + \tilde{\mu}_{\text{mol}}\left(\frac{\partial\tilde{v}_i}{\partial x_j} + \frac{\partial\tilde{v}_j}{\partial x_i}\right) \tag{5}$$

where the mass-averaged dynamic viscosity $\tilde{\mu}_{\text{mol}} = \mu_{\text{mol}}(\tilde{T})$ is determined by Sutherland's law. Similarly, the molecular heat-flux equation is

$$\bar{q}_i = -\frac{c_p\tilde{\mu}_{\text{mol}}}{Pr}\frac{\partial\tilde{T}}{\partial x_i} \tag{6}$$

with the molecular Prandtl number $Pr = 0.72$.

To close the preceding system of partial differential equations, a turbulence model needs to be introduced to determine the Reynolds-stress tensor $-\overline{\rho v_i'' v_j''}$, the turbulent heat flux $c_p\overline{\rho v_i'' T''}$, the molecular diffusion $\overline{t_{ij} v_j''}$, and the turbulent transport $\overline{\rho v_j'' v_j'' v_i''}$ (also known as triple velocity correlation).

### Turbulence Models

Turbulence models in this work are used in their original form as proposed by the respective developers. Therefore, the models will not be further outlined. Full details concerning the four turbulence models can be found in the corresponding references.[4–7]

However, two aspects of turbulence modeling that appear less frequently in the literature deserve a closer look. First, the difference in the constitutive equation for the Reynolds-stress tensor between a conventional two-equation model and an EARSM shall be briefly explained. Second, because the compressibility corrections are less widespread than the actual models the two corrections used in here will also be outlined.

#### *Modeling of the Reynolds-Stress Tensor*

The first possibility to model the Reynolds stresses is to use the Boussinesq hypothesis, as it is used in most one- or two-equation models:

$$-\overline{\rho v_i'' v_j''} = \tau_{ij} = 2\mu_T\tilde{S}_{ij} - \tfrac{2}{3}\bar{\rho}k\delta_{ij} \tag{7}$$

with

$$\tilde{S}_{ij} = \frac{1}{2}\left(\frac{\partial \tilde{v}_i}{\partial x_j} + \frac{\partial \tilde{v}_j}{\partial x_i}\right) - \frac{1}{3}\frac{\partial \tilde{v}_k}{\partial x_k}\delta_{ij} \tag{8}$$

and the eddy viscosity $\mu_T$.

It shall be noted in Eq. (7) that the Reynolds-stress tensor depends linearly on the velocity gradient. It is therefore referred to as a linear constitutive equation. In the case of an EARSM, nonlinear terms are included in the constitutive equation and it then reads

$$-\overline{\rho v_i'' v_j''} = \tau_{ij} = -\bar{\rho}k\left(a_{ij} + \tfrac{2}{3}\delta_{ij}\right) \tag{9}$$

where $a_{ij}$ is a component of the Reynolds-stress anisotropy tensor, which, using the laws of continuum mechanics for constitutive equations,[9,10] can be written as

$$\begin{aligned}\boldsymbol{a} = {} & \beta_1\boldsymbol{S} + \beta_2\left(\boldsymbol{S}^2 - \tfrac{1}{3}II_S\boldsymbol{I}\right) + \beta_3\left(\boldsymbol{W}^2 - \tfrac{1}{3}II_W\boldsymbol{I}\right) + \beta_4(\boldsymbol{SW} - \boldsymbol{WS}) \\ & + \beta_5(\boldsymbol{S}^2\boldsymbol{W} - \boldsymbol{WS}^2) + \beta_6\left(\boldsymbol{SW}^2 + \boldsymbol{W}^2\boldsymbol{S} - \tfrac{2}{3}IV\boldsymbol{I}\right) \\ & + \beta_7\left(\boldsymbol{S}^2\boldsymbol{W}^2 + \boldsymbol{W}^2\boldsymbol{S}^2 - \tfrac{2}{3}V\boldsymbol{I}\right) + \beta_8(\boldsymbol{SWS}^2 - \boldsymbol{S}^2\boldsymbol{WS}) \\ & + \beta_9(\boldsymbol{WSW}^2 - \boldsymbol{W}^2\boldsymbol{SW}) + \beta_{10}(\boldsymbol{WS}^2\boldsymbol{W}^2 - \boldsymbol{W}^2\boldsymbol{S}^2\boldsymbol{W})\end{aligned} \tag{10}$$

with the unit tensor $\boldsymbol{I}$, the mean strain tensor $S_{ij}$, and the mean rotation tensor $W_{ij}$, both normalized with the turbulent timescale $\tau = k/\epsilon$:

$$S_{ij} = \tau\tilde{S}_{ij}, \qquad W_{ij} = \frac{\tau}{2}\left(\frac{\partial \tilde{v}_i}{\partial x_j} - \frac{\partial \tilde{v}_j}{\partial x_i}\right)$$

The coefficients $\beta_1$ to $\beta_9$ appearing in Eq. (10) are functions of the invariants[2,10] $II_S$, $II_W$, $IV$, and $V$.

*Compressibility Corrections*

Although applicable to most two-equation turbulence models, the two compressibility corrections considered in the following will be used in this work for the $k$–$\omega$ model only. For the sake of completeness, the two additional transport equations for the turbulence kinetic energy $k$ and the specific dissipation rate $\omega$ are given here:

$$\frac{\partial(\bar{\rho}k)}{\partial t} + \frac{\partial(\bar{\rho}k\tilde{v}_i)}{\partial x_i} = \tau_{ji}\frac{\partial \tilde{v}_j}{\partial x_i} - \beta^*\bar{\rho}k\omega + \frac{\partial}{\partial x_i}\left[\left(\tilde{\mu}_{\text{mol}} + \sigma^*\mu_T\right)\frac{\partial k}{\partial x_i}\right] \tag{11}$$

$$\begin{aligned}\frac{\partial(\bar{\rho}\omega)}{\partial t} + \frac{\partial(\bar{\rho}\omega\tilde{v}_i)}{\partial x_i} = {} & \alpha\frac{\omega}{k}\tau_{ji}\frac{\partial \tilde{v}_j}{\partial x_i} - \beta\bar{\rho}\omega^2 \\ & + \frac{\partial}{\partial x_i}\left[(\tilde{\mu}_{\text{mol}} + \sigma\mu_T)\frac{\partial \omega}{\partial x_i}\right]\end{aligned} \tag{12}$$

with the usual model constants and coefficients of Wilcox.[4]

The $k$–$\omega$ model in its present form gives relatively accurate predictions up to supersonic speeds. In hypersonic flows, however, most two-equation models tend to overpredict the heat transfer in the reattachment region of separating boundary layers.[11] The reason for this difficulty is that $\omega$ becomes unrealistically small near the reattachment and leads to a strong growth in the turbulent length scale. (This growth does not take place with zero or one-equation models where the turbulent length scale is defined algebraically.) Vuong and Coakley[11] therefore proposed a correction for the $k$–$\omega$ model, where the turbulent length scale is limited by an algebraic length scale depending on the wall distance:

$$l = \min\left(2.5\beta^* y;\, k^{\frac{1}{2}}/\omega\right) \tag{13}$$

The new value for $\omega$ is then recomputed accordingly:

$$\omega = k^{\frac{1}{2}}/l \tag{14}$$

This correction effectively switches from a two-equation model to a one-equation model in those regions where the limit is met.

Another difficulty encountered when using two-equation models in hypersonic flows with strong compression effects is the prediction of the correct size of separation and thus the surface-pressure distribution. Again, the turbulent length scale plays a significant role in this phenomenon. In its uncorrected formulation, the $k$–$\omega$ model would predict the turbulent length scale to grow in a compression zone and to contract in an expansion zone, which is unphysical.[8] To correct this misbehavior, Coakley and Huang[8] and Vuong and Coakley[11] introduced an additional modification by increasing the coefficient multiplying the velocity divergence term in the $\omega$ equation. This term appears in the production of $\omega$ after inserting the Boussinesq approximation in Eq. (12) for the Reynolds-stress tensor. It can be written as

$$D_\omega = -\alpha\frac{2}{3}\bar{\rho}\omega\delta_{ji}\frac{\partial \tilde{v}_j}{\partial x_i} \tag{15}$$

In the high-Reynolds-number version ($\alpha \approx 0.5$) the total coefficient of this term is equal to

$$C_{D_\omega} = \alpha\tfrac{2}{3} \approx \tfrac{1}{3}$$

Based on physical arguments that are skipped here, Coakley's group[8,11] suggests that $C_{D_\omega}$ should be increased as

$$C_{D_\omega} = \tfrac{1}{3} + 1/n$$

where $n = 1, 2, 3$ for linear, cylindrical, and spherical deformations, respectively. For almost plane shock surfaces in the flows considered in the present work, wherein linear deformations are predominant, $n = 1$ is the natural choice.

In the following, these two compressibility corrections will be referred to as LS-correction (for length scale) and RC-correction (for rapid compression), respectively.

## Numerical Method

For a simply connected three-dimensional domain $V$ with a boundary $\partial V$, the Favre-averaged Navier–Stokes equations with the $k$–$\omega$ turbulence model (for example) can be written in Cartesian coordinates as

$$\begin{aligned}\int_V \frac{\partial \boldsymbol{U}}{\partial t}\,\mathrm{d}V + \oint_{\partial V}\left[(\boldsymbol{F}^c - \boldsymbol{F}^v)e_{n_x} + (\boldsymbol{G}^c - \boldsymbol{G}^v)e_{n_y}\right. \\ \left. + (\boldsymbol{H}^c - \boldsymbol{H}^v)e_{n_z}\right]\mathrm{d}A = \int_V \boldsymbol{Q}\,\mathrm{d}V\end{aligned} \tag{16}$$

where

$$\boldsymbol{U} = (\bar{\rho}, \bar{\rho}\tilde{u}, \bar{\rho}\tilde{v}, \bar{\rho}\tilde{w}, \bar{\rho}\tilde{e}, \bar{\rho}k, \bar{\rho}\omega)^T$$

is the vector of the conservative variables. The vectors $\boldsymbol{F}^c$, $\boldsymbol{G}^c$, $\boldsymbol{H}^c$ and $\boldsymbol{F}^v$, $\boldsymbol{G}^v$, $\boldsymbol{H}^v$ represent the convective and the diffusive flux functions, respectively. The complete system of partial differential equations with corresponding boundary conditions is solved numerically with the German Aerospace Center's (DLR) "FLOWer-Code"[12] (versions 114, 116) using a finite volume formulation in a block structure. The code was originally developed for the simulation of flows around airfoils in subsonic and transonic regimes. It has been extended for the simulation of hypersonic, turbulent flow problems by implementing upwind discretizations and turbulence models. Full details of these modifications can be found in Coratekin,[10] van Keuk,[13] and van Keuk et al.[14]

The flowfield is divided into nonoverlapping quadrilateral (two-dimensional) or hexahedral (three-dimensional) cells in general curvilinear coordinates $\xi$, $\eta$, $\zeta$. Equation (16) is then applied to each cell. Approximating the volume and surface integrals by the mean value theorem and the midpoint rule, Eq. (16) can be transformed into the following finite volume expression in semidiscrete

form:

$$\frac{\mathrm{d}\boldsymbol{U}_{l,m,n}}{\mathrm{d}t} = -\frac{1}{V_{l,m,n}}\left[\Delta_\xi(\hat{\boldsymbol{F}}^c - \hat{\boldsymbol{F}}^v) + \Delta_\eta(\hat{\boldsymbol{G}}^c - \hat{\boldsymbol{G}}^v) + \Delta_\zeta(\hat{\boldsymbol{H}}^c - \hat{\boldsymbol{H}}^v)\right] + \boldsymbol{Q}_{l,m,n} = \boldsymbol{Res}_{l,m,n} \tag{17}$$

$\hat{\boldsymbol{F}}$, $\hat{\boldsymbol{G}}$, and $\hat{\boldsymbol{H}}$ are the transformed flux vectors in $\xi$, $\eta$, and $\zeta$ direction, respectively, and the $\Delta_{\xi,\eta,\zeta}$ the corresponding differences [e.g., $\Delta_\xi(\,) = (\,)_{l+1/2,m,n} - (\,)_{l-1/2,m,n}$]. Following this approach, the system of partial differential equations is reduced to a system of ordinary differential equations with respect to time. It can be integrated with explicit or implicit discretization. In the FLOWer-Code, an explicit Runge–Kutta method in combination with different convergence acceleration techniques like multigrid and implicit residual smoothing is used for asymptotically steady-state solutions. In the unsteady case an implicit method based on Jameson's[15] dual time stepping is preferred for stability reasons. To increase the numerical stability of turbulent flow simulations, the time step for the turbulence equations is modiffed by a point implicit method using the source term gradient matrix. Alternatively, by decoupling the time integration of the turbulence equations from the mean equations, the turbulence equations can also be solved using alternating-direction-implicit (ADI) and diagonal-dominant ADI schemes.

To account for the directed propagation of information in the inviscid part of the equations, the convective part of the equations must be discretized with an upwind method. A large variety of different proposals exist for that purpose. Several of these techniques have been implemented into the FLOWer-Code [van Leer in the modified version of Hänel and Schwane,[16] AUSM,[1] AUSM+,[17] AUSMDV,[2] LDS,[18] HLLE,[19] Roe[3] (Harten[20]/Yee[21])], and some of them will be described more in detail in the following.

Because all upwind methods just mentioned are formally only of first-order accuracy in space, consistency with the central differences used for the diffusive terms is achieved by MUSCL-extrapolation (monotonic upstream scheme for conservation laws). Applied to the primitive and turbulent variables, it improves the formal accuracy in space of the upwind discretization to second order. To ensure the total-variation-diminishing property of the scheme flux limiters are necessary, and the one's used in this paper are Roe's "minmod" limiter and van Leer's as described by Sweby.[22]

Boundary conditions for all computations are as follows. On the inflow boundary, either freestream conditions or an incoming two-dimensional equilibrium turbulent boundary-layer profile is prescribed to match the experiment. (The boundary-layer profile is generated with Wilcox's[4] EDDYBL boundary-layer code.) On solid wall surfaces, the velocity vector and the normal gradient of static pressure $\partial_p/\partial_n$ are set to zero. The wall itself is modeled as either adiabatic or isothermal. On the top and outflow boundaries, the gradient of all conservative flow variables is set to zero.

#### AUSM Flux-Vector Splitting (Liou/Steffen)

The AUSM was originally proposed by Liou and Steffen[1] in the early 1990s. First, the inviscid flux vector is split into an advective and a pressure term. These two terms are then split separately, leading to the following expression for the flux at the cell interface:

$$\boldsymbol{F}_{l+\frac{1}{2}} = \frac{1}{2}M_{l+\frac{1}{2}}\left[\begin{pmatrix}\rho a\\ \rho a u\\ \rho a H_t\end{pmatrix}_l + \begin{pmatrix}\rho a\\ \rho a u\\ \rho a H_t\end{pmatrix}_{l+1}\right] - \frac{1}{2}\left|M_{l+\frac{1}{2}}\right|\Delta_{l+\frac{1}{2}}\begin{pmatrix}\rho a\\ \rho a u\\ \rho a H_t\end{pmatrix} + \begin{pmatrix}0\\ p_l^+ + p_{l+1}^-\\ 0\end{pmatrix} \tag{18}$$

where $\Delta_{l+1/2}\{\,\} = \{\,\}_{l+1} - \{\,\}_l$ and $M_{l+1/2} = M_l^+ + M_{l+1}^-$. The split Mach numbers $M^\pm$ are defined according to the original van Leer splitting[23]:

$$M^\pm = \begin{cases}\pm\frac{1}{4}(M \pm 1)^2, & |M| \le 1\\ \frac{1}{2}(M \pm |M|), & M > 1\end{cases} \tag{19}$$

The pressure flux terms are assumed to be governed by acoustic wave speeds. An expression using second-order polynomials of the Mach number is proposed for the pressure splitting:

$$p^\pm = \begin{cases}\frac{1}{4}p(M^\pm \pm 1)^2(2 \mp M^\pm), & |M^\pm| \le 1\\ \frac{1}{2}p[(M^\pm \pm |M^\pm|)/M^\pm], & |M^\pm| > 1\end{cases} \tag{20}$$

#### AUSMDV Flux-Vector Splitting (Wada/Liou)

Yet another approach for the splitting of the inviscid flux vector was proposed by Wada and Liou[2] as a combination of an FDS-type scheme and an FVS-type one:

$$\boldsymbol{F}_{l+\frac{1}{2}} = \begin{bmatrix}(\rho u)_{\frac{1}{2}}\\ \left(\frac{1}{2}+s\right)(\rho u^2)_V + \left(\frac{1}{2}-s\right)(\rho u^2)_D\\ (\rho u)_{\frac{1}{2}} H_t\end{bmatrix} + \begin{bmatrix}0\\ p_l^+ + p_{l+1}^-\\ 0\end{bmatrix} \tag{21}$$

where $s$ is a switch function depending on the local pressure gradient:

$$s = \frac{1}{2}\min\left[1, K\frac{|p_{l+1} - p_l|}{\min(p_l, p_{l+1})}\right] \tag{22}$$

$K$ is a paramter varying between 1.0 and 10.0. It can be seen that the AUSMD and AUSMV differ only in the treatment of the $\rho u^2$ term in the $x$-momentum flux. The corresponding expressions are

$$(\rho u^2)_V = u_l^+(\rho u)_l + u_{l+1}^-(\rho u)_{l+1} \tag{23}$$

$$(\rho u^2)_D = \tfrac{1}{2}\left[(\rho u)_{\frac{1}{2}}(u_l + u_{l+1}) - \left|(\rho u)_{\frac{1}{2}}\right|(u_{l+1} - u_l)\right] \tag{24}$$

The velocity splitting within the AUSMDV is similar to the original proposition of van Leer[23] and extended by terms designed to better capture stationary and moving contact discontinuities:

$$u_l^+ = \begin{cases}\alpha_l\left[\dfrac{(u_l + a_m)^2}{4a_m} - \dfrac{u_l + |u_l|}{2}\right] + \dfrac{u_l + |u_l|}{2} & \text{if } \dfrac{|u_l|}{a_m} \le 1\\ \dfrac{u_l + |u_l|}{2} & \text{otherwise}\end{cases} \tag{25}$$

$$u_{l+1}^- = \begin{cases}\alpha_{l+1}\left[-\dfrac{(u_{l+1} - a_m)^2}{4a_m} - \dfrac{u_{l+1} - |u_{l+1}|}{2}\right] + \dfrac{u_{l+1} - |u_{l+1}|}{2} & \text{if } \dfrac{|u_{l+1}|}{a_m} \le 1\\ \dfrac{u_{l+1} - |u_{l+1}|}{2} & \text{otherwise}\end{cases} \tag{26}$$

where

$$\alpha_l = \frac{2(p/\rho)_l}{(p/\rho)_l + (p/\rho)_{l+1}} \tag{27}$$

$$\alpha_{l+1} = \frac{2(p/\rho)_{l+1}}{(p/\rho)_l + (p/\rho)_{l+1}} \tag{28}$$

and $a_m = \max(a_l, a_{l+1})$. The pressure splitting is the same as in the original formulation, and the mass flux for the AUSMDV is

$$(\rho u)_{\frac{1}{2}} = u_l^+\rho_l + u_{l+1}^-\rho_{l+1} \tag{29}$$

**Roe's Flux-Difference Splitting (Harten/Yee)**

A sophisticated but sensitive and also more expensive flux-splitting scheme was developed by Roe.[3] Roe replaces the approximation of the solution of the nonlinear Riemann problem by the exact solution of the linearized problem, which has to be extended by the approximation of discontinuous solutions:

$$\boldsymbol{F}_{l+\frac{1}{2}} = \frac{1}{2}\left[\boldsymbol{F}^{+}_{l+\frac{1}{2}} + \boldsymbol{F}^{-}_{l+\frac{1}{2}} - \sum_{k} \alpha_k |\lambda_k| \boldsymbol{r}_k\right] \tag{30}$$

where

$$\alpha_k = \boldsymbol{l}_k\left(\boldsymbol{U}^{-}_{l+\frac{1}{2}} - \boldsymbol{U}^{+}_{l+\frac{1}{2}}\right)$$

$\lambda_k$ is the propagation speed of the $k$th wave of the linearized Riemann problem and $\boldsymbol{l}_k$, $\boldsymbol{r}_k$ are the corresponding left and right eigenvectors. The so-constructed formulation of the flux function consists of a central part supplemented by an upwind term, which has to be computed using average values of the conservative variables. One possibility for the construction of these averages is Roe averaging.

A problem appears if one of the eigenvalues changes its sign. For centered expansion fans with sonic point, the scheme leads to an expansion shock and gives unphysical solutions such as the carbuncle phenomenon in hypersonic blunt-body flows. The problem was resolved by Harten[24] with a modification of the modulus function in Eq. (31):

$$|\lambda_k| = \begin{cases} \frac{1}{2}\left(\lambda_k^2/\delta + \delta\right) & \text{for} \quad |\lambda_k| < \delta \\ |\lambda_k| & \text{else} \end{cases} \tag{31}$$

where $\delta$ is a small number often referred to as "entropy flux."

There is an alternative way of increasing the formal order of accuracy in space up to second. Originally proposed by Harten[20]/Yee,[21] it utilizes an approximation of the truncation error of the first-order scheme and is called modified flux approach.

Finally, there are many more possibilities for the splitting of the inviscid flux vector, and to the authors' experience, a very promising alternative is the low diffusion splittings (LDS) proposed by Edwards.[18]

## Results

**Validation**

The main purpose of these preliminary studies is simply to enhance confidence in the presented results for the shock/boundary-layer interactions. A complete validation of the FLOWer-Code has been performed by DLR prior to its release, and details can be found in Kroll et al.[12]

Two aspects of code validation will be considered in here. First, the numerical validation will assess such issues as convergence and grid sensitivity. Second, the physical validation will demonstrate that the turbulence models considered in the following have been properly implemented into the code.

*Numerical Validation*

For the purpose of numerical validation, a two-dimensional, 24-deg compression corner flow at Mach 3 constitutes a fair compromise between computational cost and numerical complexity. It involves a strong compression shock, a separation region, and turbulent flow, so that the computation utilized the AUSM upwind scheme and the $k$–$\omega$ turbulence model. Geometry and inflow conditions were set according to the experiments of Settles et al.[25] for the same test case.

Figure 1 shows the evolution of the density residual with respect to the number of iterations. The solution can be considered as converged after approximately 30,000 iterations. At that stage, the density residual clearly reaches its minimum value after falling for over five orders of magnitude. This relatively high number of iterations necessary to obtain a fully converged solution is caused by the hypersonic flow speed. At such conditions the convergence acceleration methods like multigrid lose much of the efficiency and might even not achieve convergence. They work very successfully in subsonic and transonic flow simulations, but a multigrid scheme particularly designed for supersonic and hypersonic flows[26] was not available in the code. In all following computations, the density residual showed a similar pattern, although the minimum value was not always reached after 30,000 iterations. The Euler computations usually required less iterations, whereas the complex crossing-shock interaction only converged after 50,000 iterations. As a precaution, 10,000 additonal iterations were always computed after the flattening of the density residual in order to ensure that the other flow variables are also converged.

**Table 1 Grid details for the viscous flow test cases**

| Quantity | Case 1 | Case 3 | Case 4 | Case 5 |
|---|---|---|---|---|
| $N_x$ | 128 | 100 | 128 | 128 |
| $N_y$ | 64 | 100 | 64 | 64 |
| $N_z$ | —— | 100 | —— | 64 |
| $\Delta x_{\min}$, m | $7.812 \times 10^{-3}$ | $1.0 \times 10^{-3}$ | $8.8 \times 10^{-5}$ | $1.0 \times 10^{-6}$ |
| $\Delta x_{\max}$, m | $7.812 \times 10^{-3}$ | $1.0 \times 10^{-3}$ | $9.6 \times 10^{-4}$ | $5.0 \times 10^{-3}$ |
| $\Delta y_{\min}$, m | $1.0 \times 10^{-6}$ | $2.0 \times 10^{-5}$ | $1.0 \times 10^{-5}$ | $1.0 \times 10^{-6}$ |
| $\Delta y_{\max}$, m | $1.0 \times 10^{-2}$ | $1.0 \times 10^{-3}$ | $8.8 \times 10^{-3}$ | $4.6 \times 10^{-3}$ |
| $\Delta z_{\min}$, m | —— | $2.0 \times 10^{-5}$ | —— | $1.0 \times 10^{-6}$ |
| $\Delta z_{\max}$, m | —— | $1.0 \times 10^{-3}$ | —— | $3.1 \times 10^{-2}$ |

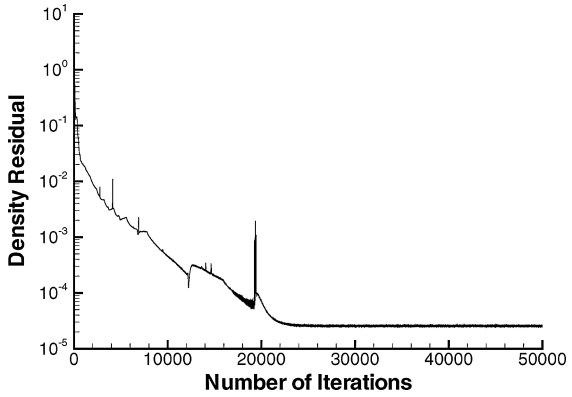


**Fig. 1 Density residual for 24-deg compression ramp (validation case).**

The next step in the numerical validation is the grid sensitivity analysis. This is necessary because one always has to make sure that the resolution is fine enough to capture the physically relevant features. As with the preceding analysis, the 24-deg compression ramp is a fair test case.

Details for the base grid can be found in Table 1. To show that this is an adequate degree of refinement, the same computation is performed on a coarser grid and on a finer grid. The base and coarse grids are actually obtained from the fine grid by including every second and every fourth grid point in each direction, respectively. Figures 2 and 3 show the results obtained on the three grids for surface pressure and skin friction. For the surface pressure, the distributions obtained with the base and the fine grid are almost identical. The coarse grid, however, shows an inaccurate pressure gradient after the initial rise at $x = -0.05$ m. Upstream of the flow deflection ($x > 0$) the coarse grid overpredicts the surface pressure by about 10%. The skin-friction distributions predicted by the base and the fine grid remain within 1% of each other up to $x = 0.05$ m. Beyond this point, the maximum discrepancy between the two grids is 5%, which is acceptable. In the same region ($x > 0.05$ m), the coarse grid predicts a significantly lower skin friction, which differs from the fine grid value by 25% at $x = 0.07$ m. According to these results, the level of refinement achieved with the base grid is sufficient to capture the relevant physics. The accuracy improvement obtained by further refinement is not important enough to justify the increase of computational cost by a factor of at least four.

Because all other test cases presented here involve similar physical features, it is assumed that a similar grid refinement in these cases

**Table 2 Freestream conditions for the viscous flow test cases**

| Quantity | Case 1 | Case 3 | Case 4 | Case 5 |
|---|---|---|---|---|
| $M_\infty$ | 5.0 | 12.3 | 9.22 | 8.3 |
| $Re_{x\infty}$, 1/m | $10^8$ | $5.0 \times 10^6$ | $4.7 \times 10^7$ | $5.3 \times 10^6$ |
| $p_\infty$, Pa | $9.2 \times 10^3$ | $1.1 \times 10^2$ | $2.3 \times 10^3$ | $4.1 \times 10^2$ |
| $T_\infty$, K | 300.0 | 45.3 | 59.44 | 75.2 |
| $T_w$, K | 327.0 | 300.0 | 295.0 | 300.0 |
| $\delta_0$, m | $10^{-4}$ | —— | 0.008 | 0.0325 |
| $\theta$, deg | —— | 8.0 | —— | —— |

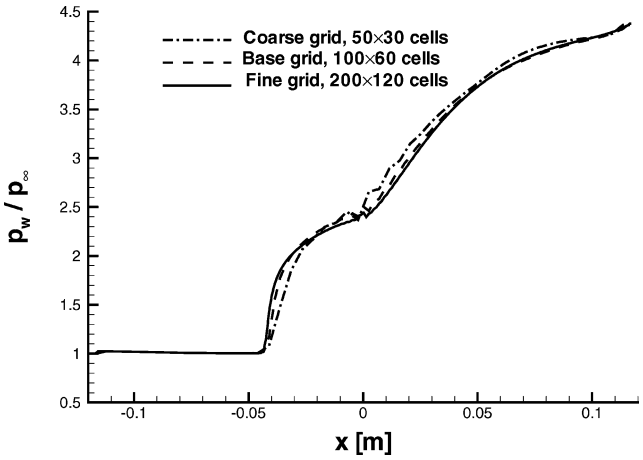


**Fig. 2 Comparison of surface-pressure distributions for 24-deg compression ramp (validation case).**

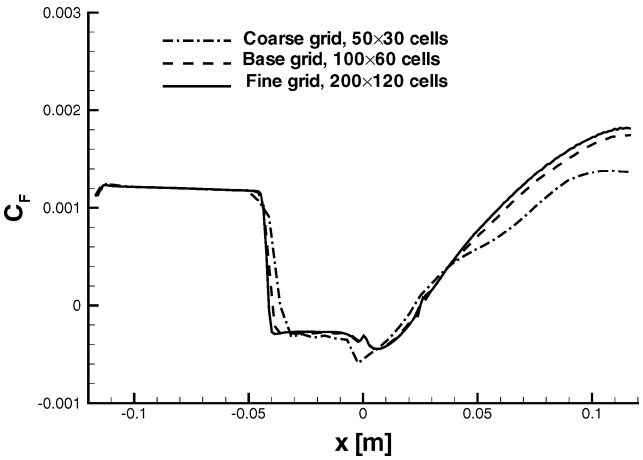


**Fig. 3 Comparison of skin-friction distributions for 24-deg compression ramp (validation case).**

will be sufficient to ensure grid-independent results. Although this assumption is obviously not entirely valid because of the nonlinearity of the governing equations, it is generally an accepted approach in engineering applications.

*Physical Validation (Case 1)*

The final step in this validation is the turbulence model validation. The most common test case for that purpose is a turbulent flow over an isothermal flat plate because results can be compared with accurate theoretical predictions. The complete set of freestream conditions for this computation are given in Table 2.

To avoid a stagnation point at the plate leading edge, the boundary condition at the inflow prescribes a very thin turbulent profile obtained with Wilcox's EDDYBL[4] boundary-layer code. The boundary-layer thickness of this thin profile is denoted $\delta_0$. This approach also allowed a uniform grid spacing in the $x$ direction. The corresponding grid details are shown in Table 1.

The method used for the validation is twofold. First, the computed skin-friction coefficients are plotted vs $x$ and compared with

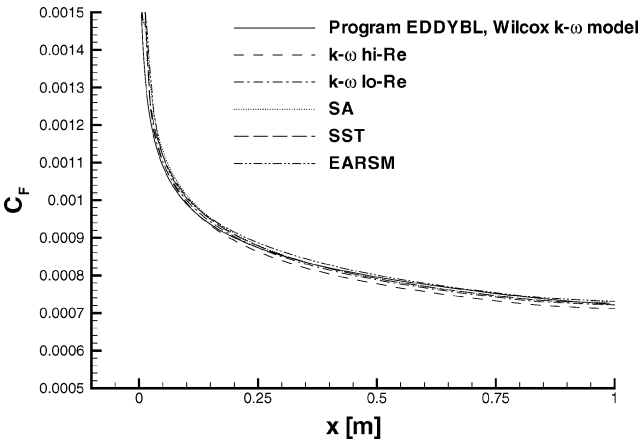


**Fig. 4 Comparison of the computed skin-friction coefficient with the EDDYBL boundary-layer code prediction.**

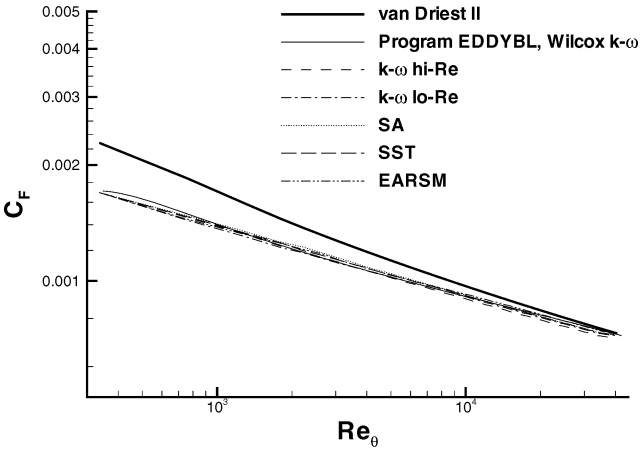


**Fig. 5 Comparison of the computed skin-friction coefficient with the van Driest II correlation.**

the corresponding EDDYBL prediction using the low-Reynolds-number $k$–$\omega$ model, which is assumed to be accurate. Second, the skin friction is compared with the van Driest II correlation for compressible boundary layers (see Ref. 27), which gives an analytical formula for $C_F$ as a function of $Re_\theta$, where $\theta$ is the momentum thickness. Results are shown in Figs. 4 and 5.

The investigated models, all used in their original form, are the high-Reynolds-number $k$–$\omega$ model, the low-Reynolds-number $k$–$\omega$ model, the Spalart–Allmaras model (SA), the SST model, and the EARSM. Although the low-Reynolds-number corrections of the $k$–$\omega$ model should not have much influence on the high-Reynolds-number flows considered in here, previous investigations by the authors showed that the low-Reynolds-number version was more stable. Therefore, only the low-Reynolds-number $k$–$\omega$ model is considered in the following shock/boundary-layer interaction flows.

The comparison of computed skin-friction distributions with the EDDYBL prediction shows that all five models give very similar results. The skin-friction coefficient is clearly within 5% of the EDDYBL prediction. The second comparison with the van Driest II correlation shows that all models, including the EDDYBL $k$–$\omega$ model, underpredict the skin-friction coefficient. For $Re_\theta < 10^3$, the discrepancy is over 30%. However, although this might sound alarming one has to keep in mind that the scaling in $Re_\theta$ is logarithmic and that the region where $Re_\theta$ is below $10^4$ corresponds to $x < 0.1$ m. Thus, the differences between the computed results and the correlation are above 5% in the initial region of the boundary-layer only. Once the boundary layer is fully developed, the predictions are in good agreement with the theory.

The main point of this section was to validate the turbulence models implemented in the modified FLOWer-Code. The results show

that this goal has obviously been achieved. The relative performance of the turbulence models for the flat-plate flow is not considered here, and so further discussion is omitted for the sake of brevity.

### Influence of the Upwind Scheme

*Euler Flows (Case 2)*

Hypersonic flows over double-wedge geometries are interesting test cases to assess the capability of upwind methods to predict and resolve shocks and contact surfaces. One such flow has recently been investigated by Olejniczak et al.[28] which serves here as a reference case. The freestream Mach number is 9.0, and the wedge angles are $\Theta_1 = 15.0$ deg and $\Theta_2 = 45.0$ deg. The highly complex flow-field consists of seven shock waves and three contact surfaces and is known as a type V interaction. Figures 6 and 7 show a comparison for the computed Mach-number distribution with the reference solution.[28] The qualitative agreement regarding the major flow phenomena and the distribution of subsonic and supersonic regions is quite satisfying. It is worth mentioning that the computational grid used in the present work consisted of 320.000 grid points, whereas Olejniczak et al.[28] used 1.048.576 grid points.

A comparison of the results obtained with AUSM and AUSMDV is shown in Figs. 8 and 9. The clearly visible pressure oscillations behind the shock waves are an indication for the nonmonotone behaviour of the AUSM method across shocks. In addition, pressure disturbances are not damped by the scheme, and the pressure oscillations appearing near the walls could be a consequence of this.

Finally, Figs. 10 and 11 show the often not addressed influence of the flux limiter. Both calculations have been carried out with the AUSMDV splitting on the same computational grid. As a consequence of the less viscous van Leer limiter, the big shear layer resulting from the interaction point becomes unstable, leading to clearly visible vortex structures. To the contrary, the shear layer remains stable when using the minmod limiter. The authors assess the unstable solution to be the physically more relevant one as a result of instability waves occuring at high-speed jets. There exist three families of instability waves as detected by Oertel[29] and discussed analytically and computationally by Tam and Hu.[30] One of them is the Kelvin–Helmholtz instability, and the two others are governed by acoustic waves and denoted as supersonic and subsonic instability.

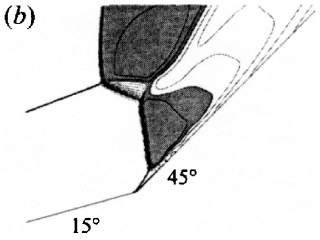


**Fig. 6 Type V shock interaction, Mach contours of Olejniczak et al.,[28] with subsonic regions shaded.**

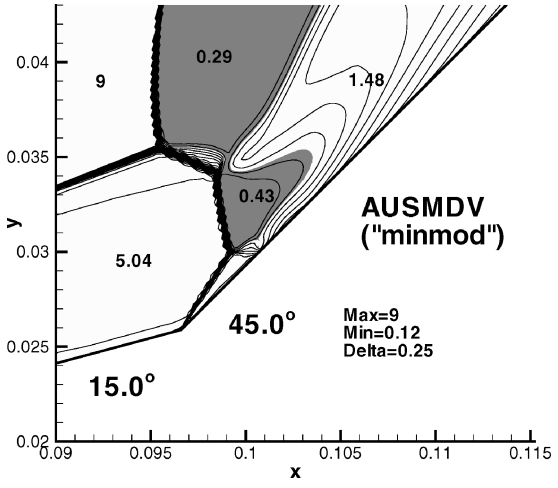


**Fig. 7 Type V shock interaction: Mach contours from present work using AUSMDV scheme, with subsonic regions shaded.**

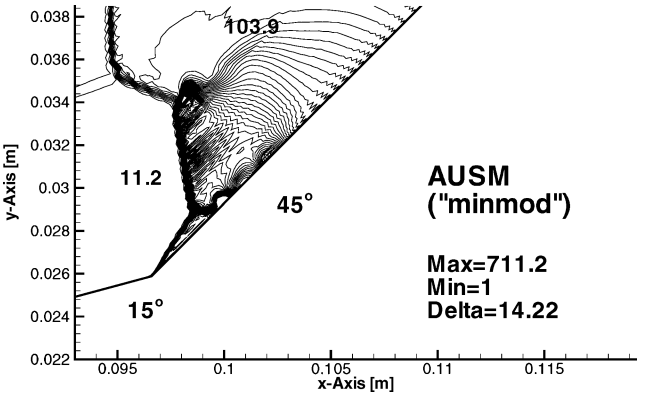


**Fig. 8 Type V shock interaction: pressure contours using AUSM scheme.**

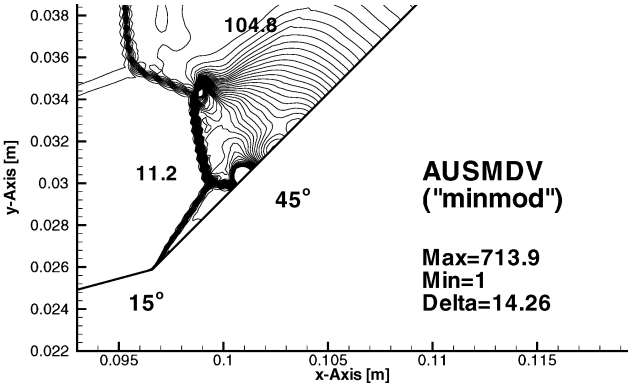


**Fig. 9 Type V shock interaction: pressure contours using AUSMDV scheme.**

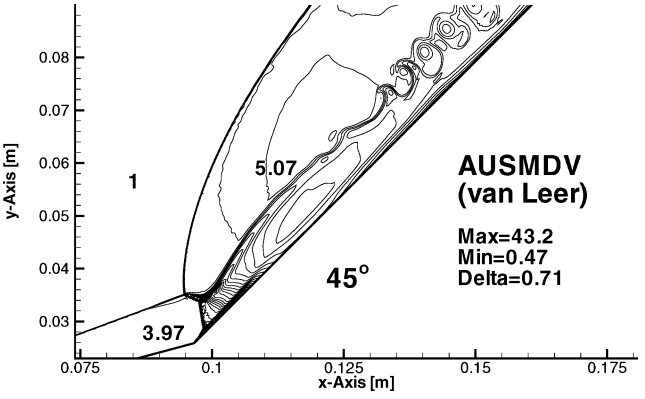


**Fig. 10 Type V shock interaction: density contours, influence of the flux limiter.**

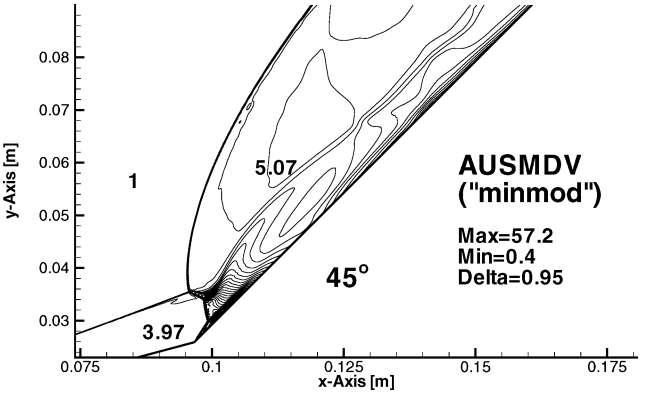


**Fig. 11 Type V shock interaction: density contours, influence of the flux limiter.**

*Laminar Navier–Stokes Flows (Case 3)*

This section considers the three-dimensional flow in a symmetric corner formed by two wedges with angle $\theta = 8$ deg in the laminar regime. This configuration has been studied in detail in the literature, so that a comparison with both numerical and experimental results of other authors can be presented. Freestream conditions are set to the same values as in Kipke and Hummel's[31] experiment and are given in Table 2, where $\theta$ denotes the wedge angle. Details of the grid used are shown in Table 1.

Figures 12 and 13 show the computed Mach-number contours for Roe's scheme, compared with those of D' Ambrosio et al.[32] There is a system of five shocks in total. Two of them are the primary shocks generated by the wedged sidewalls on the left and bottom side of the computational domain. The other three shocks are caused by the Mach disk (irregular reflection) in the corner, where the primary shocks interact. Two contact discontinuities, generated by the different conditions on each side of the interactions, stretch from the triple points to the symmetry plane. In addition, two reflected shock waves interact with the boundary layers and are reflected as expansion fans, which are transformed in compression waves when interacting with the contact discontinuities. The impinging shocks cause the boundary layers to separate, thus producing two vortex systems. As in Kipke and Hummel's[31] experiment, Mach-number contours are plotted for a cross section at $x = 0.09$ m. All of the physical flow phenomena, even the secondary separation, are qualitatively well resolved in both cases. This is quite satisfactory considering the fact that both cases used different grids, different computational domains, and in particular completely different numerical codes. The computation of D' Ambrosio et al.[32] solved the parabolized Navier–Stokes equations using a space marching method on a computational grid consisting of $120 \times 120$ cells.

Figures 14 and 15 show a comparison of the results obtained with the original AUSM an AUSMDV schemes for Mach number and pressure distributions. The original AUSM gives the best resolution of the secondary separation because the scheme has the lowest artificial viscosity.

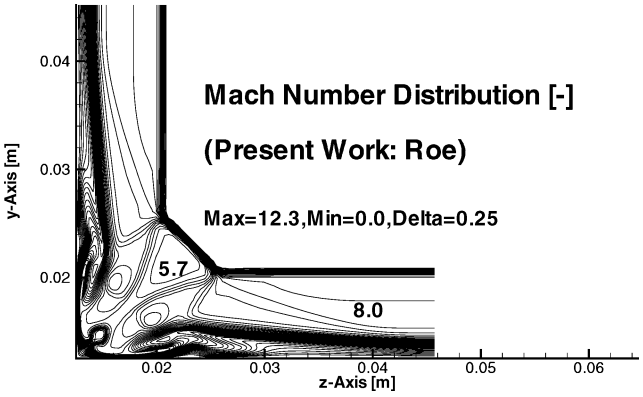


**Fig. 12 Computed results for Mach-number distribution (present work), where $x = 0.09$ m.**

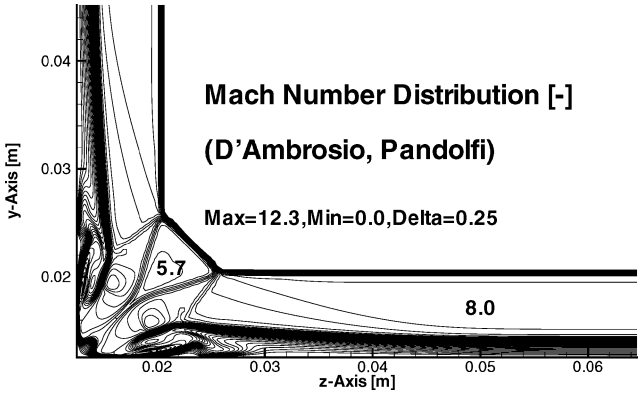


**Fig. 13 Computed results for Mach-number distribution (D' Ambrosio et al.[32]), where $x = 0.09$ m.**

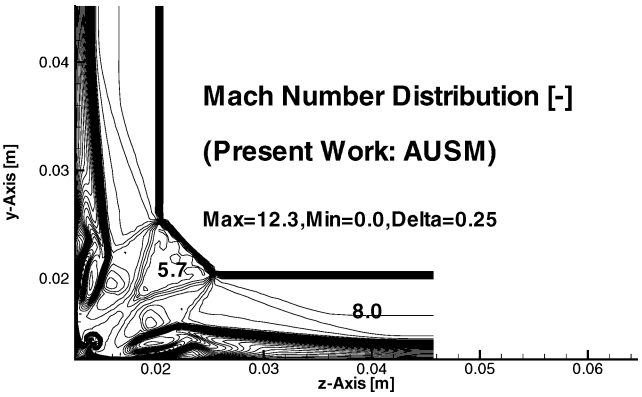


**Fig. 14 Computed results for Mach-number distribution (present work, AUSM), where $x = 0.09$ m.**

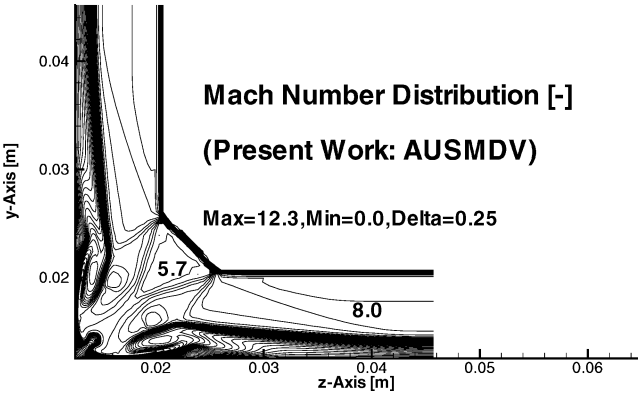


**Fig. 15 Computed results for Mach-number distribution (present work, AUSMDV), where $x = 0.09$ m.**

A comparison of all numerical results with the experimental data of Kipke and Hummel[31] is provided in Figs. 16 and 17 for the wall pressure at ($x = 0.09$ m). The overall agreement between the measured and computed values is fairly satisfying. Results of D' Ambrosio et al.[32] predict a slightly more accurate distribution in the reattachment zone, but this can be attributable to the smaller computational domain chosen in the present work, namely, $0.0455 \times 0.0455$ m in place of $0.065 \times 0.065$ m (see Figs. 12, 14, and 15 with Fig. 13). In addition, the region of the secondary separation and the near-wall region are enlarged in Figs. 17 and 18. It can be seen that the results of the present work are in better agreement with the experiment near the wall. A possible reason for this can be the three-dimensionality of the flow and the subsonic Mach numbers near the wall, where a three-dimensional-full Navier–Stokes simulation should give better results than a space-marching method for the parabolized equations. In the secondary separation region, results obtained with AUSM and AUSMDV are in good agreement with the experiment and with the results of D' Ambrosio et al.[32] For the computation with Roe's scheme, the entropy fix parameter had to be set to 0.1 for stability reasons. As a consequence, the pressure maximum is more smeared out.

#### Influence of the Turbulence Model

According to the investigation carried out in the preceding section, the most suitable upwind schemes for hypersonic shock/boundary-layer interactions are the AUSM and the AUSMDV. In the following turbulent computations, it is important that the scheme has minimal numerical viscosity because turbulence already increases overall viscosity. All physical phenomena that are linked to viscosity, especially separation, should thus be attributable to physical viscosity (molecular and eddy) only. Therefore, results in the next two sections were all computed using the AUSM scheme, which has the lowest

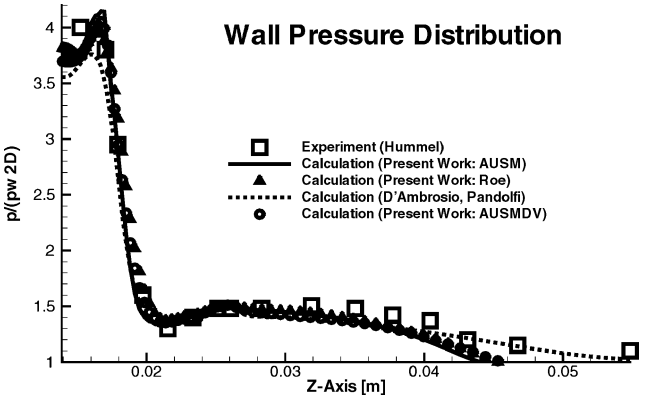


**Fig. 16 Wall-pressure distribution (calculations/experiment).**

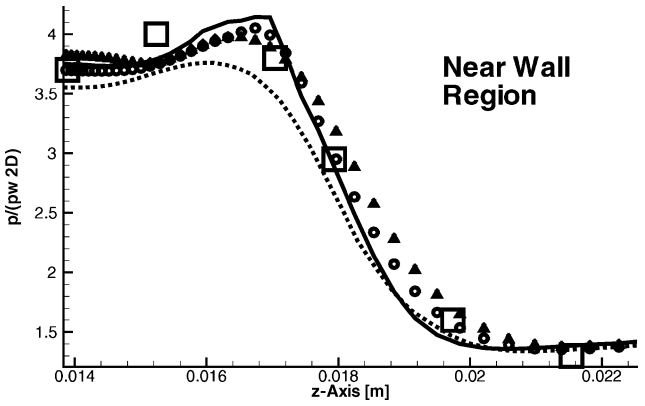


**Fig. 17 Wall-pressure distribution for the near-wall region (calculations/experiment).**

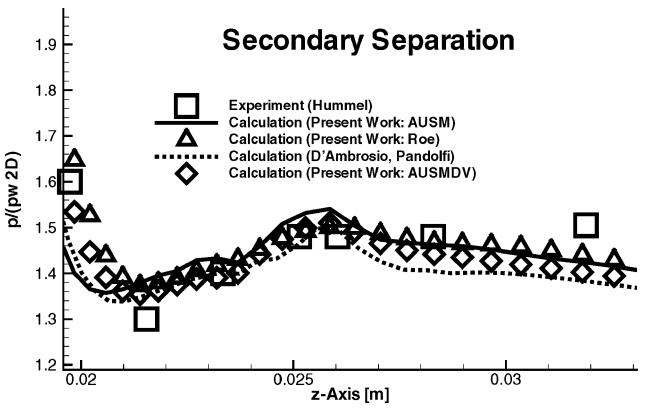


**Fig. 18 Wall-pressure distribution for the secondary separation area (calculations/experiment).**

numerical viscosity.[33,34] The more superior AUSMDV scheme will be tested in future work in order to assess whether or not the original AUSM's pressure oscillations near the wall, or the AUSMDV's slightly higher numerical viscosity have a significant influence on the results.

*Two-Dimensional Compression Ramp (Case 4)*

The experiment of Coleman and Stollery[35] for a 38-deg compression ramp at Mach 9.22 according to Fig. 19 serves as a test case for a hypersonic shock/boundary-layer interaction. This is a quite difficult test case because it involves a very strong compression as a result of the high ramp angle. At these Mach numbers, a minimum ramp angle of 31 deg is required to obtain a significant boundary-layer separation. The experiment was performed in a hypersonic gun tunnel using nitrogen as a test gas. This is taken into account

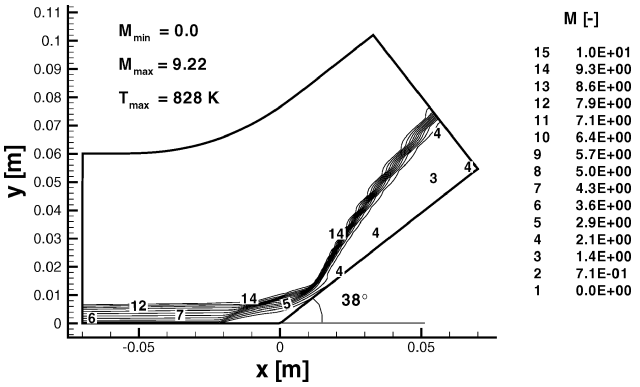


**Fig. 19 Mach-number contours obtained with the low-Reynolds-number $k$–$\omega$ model.**

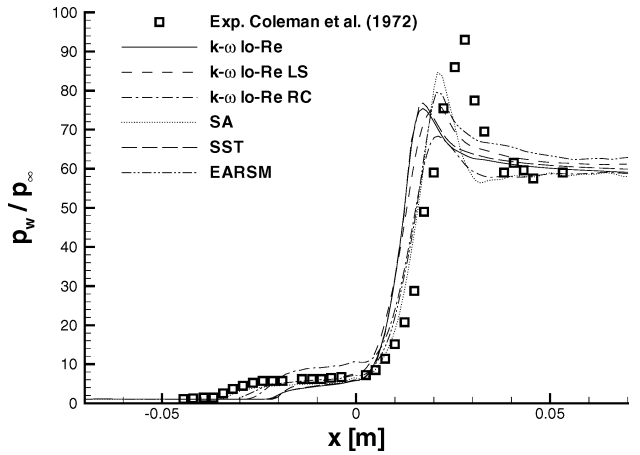


**Fig. 20 Comparison of computed surface pressure with experimental data.**

in the numerical simulations by adjusting the perfect-gas constant and the constants in Sutherland's law. The freestream conditions are given in Table 2, and grid details can be found in Table 1, where $\delta_0$ represents the boundary-layer thickness at the inflow boundary.

Six different turbulence models were used in this test case: the low-Reynolds-number $k$–$\omega$ model ($k$–$\omega$ lo-Re), the low-Reynolds-number $k$–$\omega$ model with the length scale correction ($k$–$\omega$ lo-Re LS), the low-Reynolds-number $k$–$\omega$ model with the rapid compression correction ($k$–$\omega$ lo-Re RC), the Spalart–Allmaras model (SA), the SST model, and the EARSM. In all computations, the wall temperature was set to the constant value of 295 K as measured in the experiment.

Because of the high level of compressibility in this flow, the various turbulence models behave quite differently, particularly in the reattachment zone, as can be seen in Figs. 20 and 21. The exact experimental uncertainties for surface-pressure and heat-flux measurements were not mentioned in the original papers, but it can be assumed that they lie within $\pm 5$ and $\pm 15\%$, respectively. Figure 20 shows the computed surface-pressure distribution in comparison with experimental values. The initial pressure rise corresponds to the separation point. Obviously the $k$–$\omega$ lo-Re, $k$–$\omega$ lo-Re LS, and SST models separate too far downstream and predict a smaller separation than in the experiment. Improvement for the $k$–$\omega$ lo-Re models is obtained by including the rapid compression correction ($k$–$\omega$ lo-Re RC model). This causes the flow to separate earlier, but still not far enough upstream. The apparent drawback of this correction is an overprediction of the initial pressure rise, which has not been observed by other authors,[36] and so further research might be necessary to assess the influence of the rapid compression correction on this type of flow. The EARSM displays an increased separational behavior that proves to be beneficial in hypersonic flows, as the predicted separation point is relatively close to the experiment. The

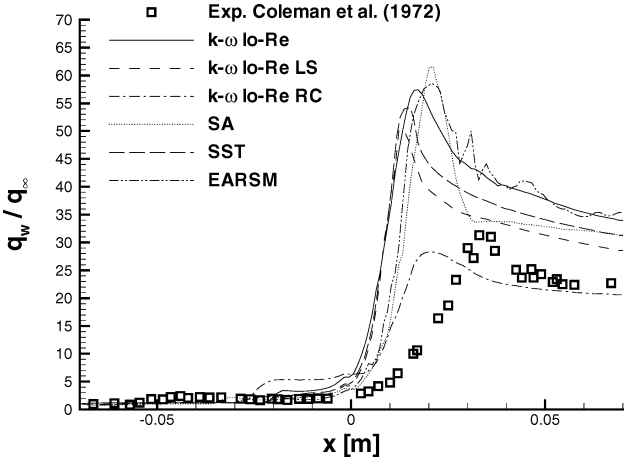


**Fig. 21 Comparison of computed heat transfer with experimental data.**

most surprising result, however, is the exceptionally good performance of the SA model, which separates almost exactly as predicted by the experiment.

Downstream of the ramp corner, the pressure rise caused by the shock wave is underpredicted by each model. Again, the pressure peak predicted by the SA model comes closest to the experimental value, followed by the EARSM. The $k$–$\omega$ lo-Re RC model gives the lowest pressure rise. This is consistent because the boundary-layer computed with the $k$–$\omega$ lo-Re RC model has lost more energy in the separation than the other two $k$–$\omega$ models. The gradient of that rise is in fairly good agreement with the experiment for the $k$–$\omega$ lo-Re RC model, the SA model, and the EARSM. The other models generate a steeper gradient that is slightly corrected with the $k$–$\omega$ lo-Re LS model. Downstream of the primary shock wave, in the reattached flow region, the $k$–$\omega$ lo-Re, $k$–$\omega$ lo-Re RC, SA, and SST models predict surface-pressure values that are quite close to the measured ones. However, the EARSM slightly overpredicts the pressure plateau.

The heat-transfer distributions are shown in Fig. 21. The initial rise in heat transfer occurs at approximately $x = -0.055$ m. All models predict that rise too far downstream. The order in which the models produce a rise in heat transfer is similar to the order in which they predict the corresponding pressure rise. However, the magnitude of that rise is overpredicted by the $k$–$\omega$ lo-Re model and the $k$–$\omega$ lo-Re RC model. (As for the pressure rise, this apparently unphysical prediction of the $k$–$\omega$ lo-Re RC model has not been observed by other authors.[36]) At $x = 0$, the measured heat transfer undergoes a significant rise but at a relatively moderate rate. Both the gradient and the magnitude of that rise are dramatically overpredicted by all models. The rapid compression correction is beneficial for the predicted magnitude but gives only minor improvements for the gradient. As for the surface pressure, the SA model gives the highest peak value, followed by the EARSM, the $k$–$\omega$ lo-Re, the SST, and the $k$–$\omega$ lo-Re LS models. In the reattachment region, the $k$–$\omega$ lo-Re RC obviously performs best because it predicts a reasonable value for the heat-transfer rise. As expected, the $k$–$\omega$ lo-Re LS shows some improvement compared with the $k$–$\omega$ lo-Re as it predicts a significantly lower heat transfer. The SST model gives heat-flux values that are more or less in between those predicted with the $k$–$\omega$ lo-Re and $k$–$\omega$ lo-Re LS models. Noteworthy are the instabilities featured by the EARSM, which have also been observed by the authors for other high-Mach-number flows.[37]

This complex test case shows the strength and weaknesses of the various models in hypersonic flows with high compression. The SA model appears to have certain features that enable it to give good predictions for the surface pressure. The EARSM still generates more separation than the other models, which is quite beneficial in hypersonic flows. As opposed to the supersonic compression corner, the standard $k$–$\omega$ model obviously needs to be corrected in order to predict more separation. The rapid compression correction, although not perfect, partially achieves this goal. Regarding heat-transfer prediction capability, all standard models generally predict far too much heat flux. The compressibility corrections for the $k$–$\omega$ model, especially the rapid compression correction, give significantly better results. The instabilities observed with the EARSM seem to be a major drawback of this model. It should, however, be mentioned that some of the discrepancies observed in this test case could be attributed to insufficient grid refinement on the ramp. Further investigations are therefore necessary to assess this possibility.

*Three-Dimensional Crossing-Shock Interaction (Case 5)*

The hypersonic crossing-shock interaction investigated in this study is symmetric, and the two fin angles are equal to 15 deg. The experiment was conducted at a freestream Mach number of 8.3 by Kussoy et al.[38] Figure 22 shows the geometry for this test case. The full set of freestream conditions is given in Table 2, where $\delta_0$ represents the boundary-layer thickness at the fin leading edge. The corresponding grid details are given in Table 1. This level of refinement is comparable to the one used by other authors[39,40] for the same test case.

Four turbulence models were tested on this flow: the low-Reynolds-number $k$–$\omega$ model ($k$–$\omega$ lo-Re), the low-Reynolds-number $k$–$\omega$ model with the length scale correction ($k$–$\omega$ lo-Re LS), the low-Reynolds-number $k$–$\omega$ model with the rapid compression correction ($k$–$\omega$ lo-Re RC), and the Spalart–Allmaras model (SA). For each computation, all walls were assumed isothermal with $T_w = 300$ K. On the symmetry plane ($xy$ plane), the normal component of velocity and the normal derivatives of the remaining flow variables were set equal to zero.

Surface-pressure distributions on the channel's bottom middle line and at streamwise cross section ($x = 0.225$ m) are displayed in Figs. 23 and 24. The assigned experimental uncertainty in the pressure measurements is $\pm 5\%$. All turbulence models show relatively good agreement with the experiment. On the channel middle line, the models fail to predict the slight change in curvature measured in the experiments at $0.10 \text{ m} < x < 0.16$ m. The SA model generally predicts a higher surface pressure than the $k$–$\omega$ models with a peak value 5% above the highest experimental value. Up to $x = 0.2$ m, all three $k$–$\omega$ models show no differences. Farther downstream, the $k$–$\omega$ lo-Re LS model produces a higher surface pressure than the $k$–$\omega$ lo-Re and gives the most accurate prediction for the peak value. The rapid compression correction has a minor effect only.

On the streamwise cross section at $x = 0.225$ m, both corrections for the $k$–$\omega$ lo-Re slightly increase the surface pressure. The high pressure values are best predicted with the $k$–$\omega$ lo-Re LS model. Near the side walls, where the separation is less important, the SA model gives the lowest pressure values and is in good agreement with the experiment.

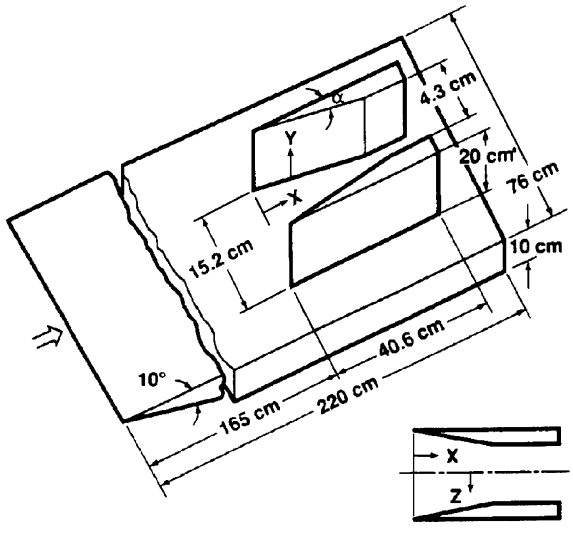


**Fig. 22 Flow geometry for crossing-shock interaction.**

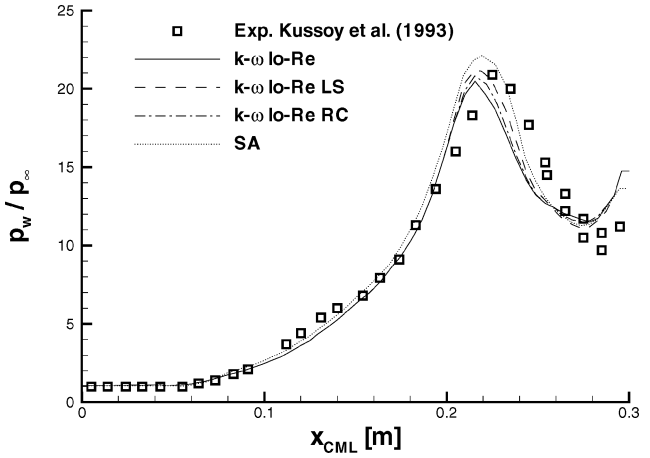


**Fig. 23 Comparison of computed surface pressure on the channel middle line with experimental data.**

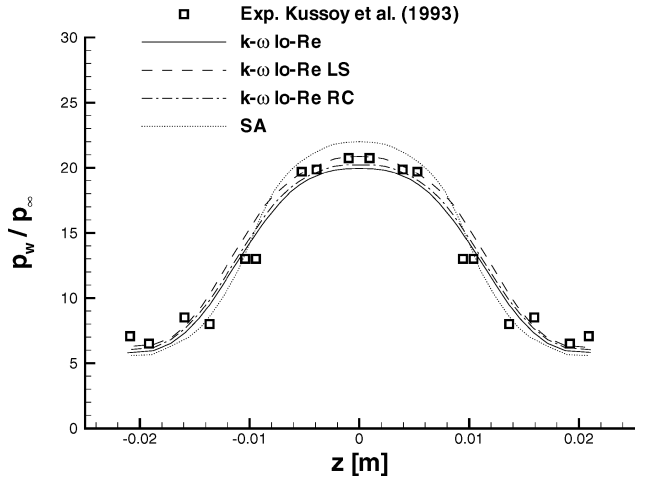


**Fig. 24 Comparison of computed surface pressure at a streamwise cross section with experimental data ($x = 0.22$ m).**

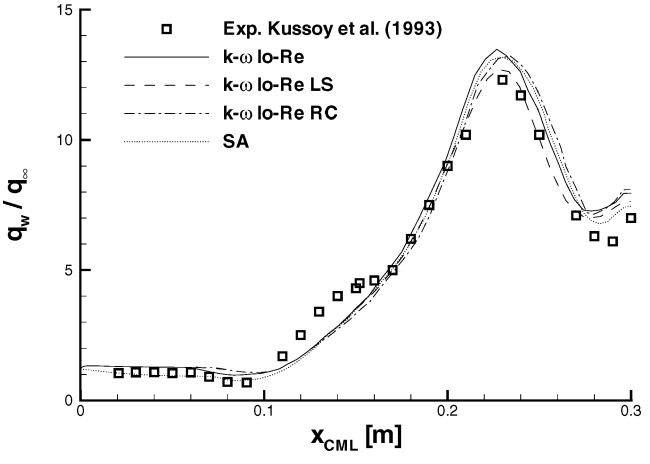


**Fig. 25 Comparison of computed heat transfer on channel middle line with experimental data.**

Surface heat-transfer distributions are shown in Figs. 25 and 26. The experimental uncertainty is $\pm 10\%$. On the channel middle line, the general agreement with the experiment is similar to that observed for the surface pressure. In the undisturbed flow region, $x < 0.1$ m, the SA predictions are in good agreement with the experiment. (The value of $q_w/q_\infty$ is a little higher than the expected value of one for all models. This is because of an adjustment of the flow variables to the boundary-layer profile prescribed at the inflow boundary.) That model also captures the initial heat-transfer drop quite well. As for

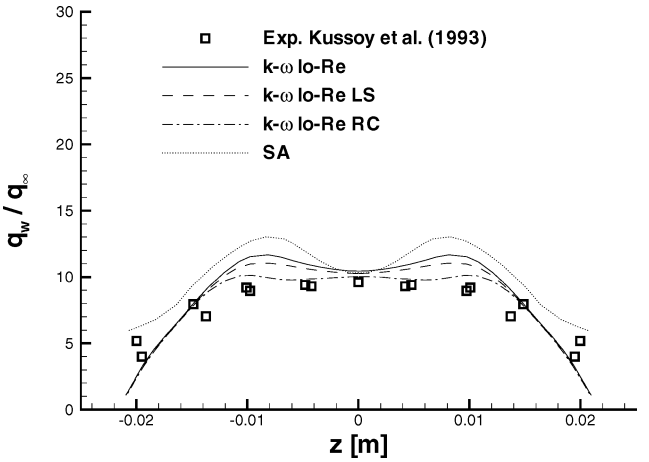


**Fig. 26 Comparison of computed heat transfer at $x = 0.205$ m with experimental data.**

the surface pressure, the convex curvature of the heat-transfer rise at $0.10 \text{ m} < x < 0.16$ m is not captured by any of the turbulence models. Up to $x = 0.22$ m, both compressibility corrections for the $k$–$\omega$ model and the SA model predict a lower heat transfer than the $k$–$\omega$ lo-Re model. The corrections start having an effect on the solution downstream for $x \geq 0.15$ m. The best agreement for the peak value is obtained with the $k$–$\omega$ lo-Re LS model. The SA and $k$–$\omega$ lo-Re RC models give approximately the same peak value, which is 10% above the measured value, and the $k$–$\omega$ lo-Re model gives the maximum deviation for the peak value (13%). The heat transfer drops down downstream of $x = 0.22$ m, where the $k$–$\omega$ lo-Re LS model still gives the best agreement with experiment. The SA and $k$–$\omega$ lo-Re RC models display very similar behavior in that region as they both overpredict the heat transfer by approximately 10%. The predictions of the $k$–$\omega$ lo-Re model lie in between those for the $k$–$\omega$ lo-Re LS and SA models.

The deviations from experiment are significantly greater in Fig. 26, which shows the heat-transfer distributions at a streamwise cross section ($x = 0.205$ m). This is because the major separations do not take place on the channel middle line but on the right- and left-hand side of it. In those regions, the SA model overpredicts the measured heat transfer by almost 30%. The $k$–$\omega$ lo-Re model gives a somewhat lower heat transfer but is still off by 20%. The length-scale correction and the rapid-compression correction both reduce the heat transfer at $z = \pm 0.01$ m by 10 and 20%, respectively. Thus, the $k$–$\omega$ lo-Re RC model gives the best agreement with the experiment. Near the side walls, all three $k$–$\omega$ models behave identically, whereas the SA model still overpredicts the heat transfer by 20% on the average.

Because of the relatively high experimental uncertainty, conclusions on the performance of the turbulence models should be made with care. For example, if the "real" value of the peak heat transfer in Fig. 25 is 10% higher than the one shown, the uncorrected $k$–$\omega$ model would give the most realistic prediction. However, the following relative conclusions are possible for this type of flow. The SA model generally predicts higher surface pressure and lower heat transfer than the $k$–$\omega$ lo-Re model. In this context another compressibility correction was proposed by Spalart[41] for this model. Studying the influence and properties of this correction will be subject of future work. In highly separated areas, however, it overpredicts the heat transfer considerably. The length-scale and rapid-compression corrections generally give higher surface pressure values and less heat transfer than the uncorrected $k$–$\omega$ model. However, when the heat transfer drops down on the channel middle line the $k$–$\omega$ lo-Re RC model actually predicts a higher heat transfer than the $k$–$\omega$ lo-Re model.

## Conclusions

Three upwind schemes and four turbulence models were investigated in hypersonic flows using a block-structured, explicit

finite volume flow solver. The convective part of the balance equations was discretized using either the advection upstream splitting method (AUSM), the AUSMDV, or the Roe scheme. With MUSCL-extrapolation the formal accuracy in space was increased to second order. Total-variation-diminishing property of the scheme was ensured by applying an appropriate limiter, whose influence was also assessed. In turbulent flow computations, the Favre-averaged Navier–Stokes equations were solved in combination with a turbulence model. Four models were investigated herein: Wilcox's $k$–$\omega$ model, the Spalart–Allmaras model, Menter's supersonic transport (SST) model, and an explicit algebraic Reynolds-stress model by Wallin and Johansson. Additionally, two compressibility corrections for the $k$–$\omega$ model of Coakley and his group have also been tested. Numerical results were compared with corresponding experimental data or results computed by other authors.

In an initial step, the influence of the upwind scheme alone was assessed for a two-dimensional Euler flow at Mach 9. The double-wedge configuration is an interesting hypersonic test case involving complex shock/shock interactions. The overall agreement with other numerical results was quite satisfactory. The AUSM scheme gave the most accurate results in terms of shock resolution because it has the lowest numerical viscosity. However, it displays spurious pressure oscillations in the vicinity of shock waves and near solid walls. The AUSMDV scheme does not show such behavior but is therefore more dissipative. The influence of the limiter was also quite interesting to note. Downstream of the shock interaction point, the van Leer limiter produces a shear-layer instability, whereas the shear layer remains stable when using the minmod limiter. Which one of both is closer to reality cannot be said because experimental data for this test case were unavailable.

The second test configuration was a three-dimensional corner flow at Mach 12. Results of the laminar Navier–Stokes computation were compared with experimental data. The agreement for the surface-pressure distribution is very good. Again, the AUSM scheme proved to be the most accurate of all but displayed similar pressure oscillations as in the Euler case. Those oscillations were damped by the more viscous AUSMDV scheme. The Roe scheme was stable only when the entropy fix parameter was set to 0.1 or higher, which considerably increases the numerical viscosity. Thus, the secondary separation was less accurately resolved. It was also proved to be computationally expensive, particularly for three-dimensional computations. Compared with calculations using AUSMDV Roe's method requires around 30% more computer time for two-dimensional cases and around 60% more computer time for three-dimensional cases, respectively. It seems that the AUSM and AUSMDV are the most suited upwind schemes for hypersonic flows of engineering interest.

In view of the just mentioned, the last test cases that involve turbulence were computed using the AUSM scheme. The first was a two-dimensional compression corner flow at Mach 9, which had been investigated experimentally by other authors in the past. Its major difficulty lies in the strong compression and large flow separation caused by the relatively high ramp angle of 38 deg. The second test case is known as crossing-shock interaction and is a typical example of a three-dimensional turbulent shock/boundary-layer interaction. Computed results for surface pressure and surface heat transfer were compared with measurements. Whereas the overall agreement was quite acceptable and within the experimental uncertainty, difficulties arise whenever the flowfield becomes very complex and involves large-scale separation. Based on these and other results published by the authors, the following conlusions on the applicability of turbulence models in hypersonic flows can be made.

In general, it has been found that the surface pressure is relatively well predicted by all turbulence models. In simpler cases, like a supersonic compression ramp or the symmetric crossing-shock interaction, the models also give satisfactory agreement with experiment for skin friction and heat transfer. Major problems appear, however, when investigating more complex flows with stronger compression or separated flowfields. Along the hypersonic compression ramp, for example, the flow undergoes an extremely high compression. The Spalart–Allmaras model was the only model to predict the right separation and a high enough rise in the surface pressure. For the surface heat transfer, only the $k$–$\omega$ model in combination with the rapid-compression correction was able to give results within an error of 10% of the experimental value behind the shock. Regarding computational cost per iteration, the one-equation Spalart–Allmaras model requires approximately 15% less CPU time than the $k$–$\omega$ model, whereas the SST and EARSM need 10 and 25% more CPU time, respectively.

## Acknowledgments

This work was sponsored by the Deutsche Forschungsgemeinschaft within the frames of the Collaborative Research Center SFB 253 "Fundamentals of Design of Aerospace Planes" and the Graduiertenkolleg 5/3 "Transport Phenomena in Hypersonic Flows." The very helpful and constructive comments of the anonymous reviewers are appreciated as well.

## References

[1]Liou, M. S., and Steffen, C. J., "A New Flux Splitting Scheme," *Journal of Computational Physics*, Vol. 107, 1993, pp. 23–39.

[2]Wada, Y., and Liou, M. S., "An Accurate and Robust Flux Splitting Scheme for Shock and Contact Discontinuities," *SIAM Journal on Scientific Computing*, Vol. 18, 1997, pp. 633–648.

[3]Roe, P. L., "Approximate Riemann Solvers, Parameter Vectors, and Difference Schemes," *Journal of Computational Physics*, Vol. 43, 1981, pp. 357–372.

[4]Wilcox, D. C., *Turbulence Modeling*, DCW Industries, La Canada, CA, 1994.

[5]Spalart, P. R., and Allmaras, S. R., "A One-Equation Turbulence Model for Aerodynamic Flows," AIAA Paper 92-0439, Jan. 1992.

[6]Menter, F. R., "Two-Equation Eddy-Viscosity Turbulence Models for Engineering Applications," *AIAA Journal*, Vol. 32, No. 8, 1994, pp. 1598–1605.

[7]Wallin, S., and Johansson, A. V., "A New Explicit Algebraic Reynolds Stress Turbulence Model," *Journal of Fluid Mechanics*, Vol. 403, 2000, pp. 89–132.

[8]Coakley, T. J., and Huang, P. G., "Turbulence Modeling for High Speed Flows," AIAA Paper 92-0436, Jan. 1992.

[9]Jaunzemis, W., *Continuum Mechanics*, Macmillan/McGraw–Hill, New York, 1967.

[10]Coratekin, T. A., "Numerical Simulation of Turbulent Shock/Boundary-Layer Interactions in Hypersonic Flows," *Strömungstechnik, Fortschritt-Berichte*, Vol. 7/381, Verein Deutscher Ingenieure, Dusseldorf, Germany, 2000, pp. 1–96.

[11]Vuong, S. T., and Coakley, T. J., "Modeling of Turbulence for Hypersonic Flows with and Without Separation," AIAA Paper 87-0286, Jan. 1987.

[12]Kroll, N., Raddatz, J., and Heinrich, R., "FLOWer Version 114.1," Inst. für Entwurfsaerodynamik—Deutsches Zentrum für Luft- und Raumfahrt, DLR, German Aerospace Center, Braunschweig, Germany, 1997.

[13]van Keuk, J., *Numerische Analyse und Bewertung von Upwind-Verfahren für die Anwendung auf mehrdimensionale Über- und Hyperschallströmungen von Gasen*, Springer-Verlag, Berlin, 2000; also Ph.D. Dissertation, Dept. of Mechanical Engineering, RWTH Aachen, Aachen, Germany, June 2000.

[14]van Keuk, J., Ballmann, J., Schneider, A., and Koschel, W., "Numerical Simulation of Hypersonic Inlet Flows," AIAA Paper 98-1526, April 1998.

[15]Jameson, A. J., "Time Dependent Calculation Using Multigrid, with Application to Unsteady Flows past Airfoils and Wings," AIAA Paper 91-1596, June 1991.

[16]Hänel, D., and Schwane, R., "An Implicit Flux-Vector Splitting Scheme for the Computation of Viscous Hypersonic Flow," AIAA Paper 89-0274, Jan. 1989.

[17]Liou, M. S., "A Sequel to AUSM: AUSM+," *Journal of Computational Physics*, Vol. 129, 1996, pp. 364–382.

[18]Edwards, J. R., "A Low-Diffusion Flux-Splitting Scheme for Navier–Stokes Calculations," *Computers and Fluids*, Vol. 26, No. 6, 1997, pp. 635–659.

[19]Harten, A., Lax, P. D., and van Leer, B., "On Upstream Differencing and Godunov-Type Schemes for Hyperbolic Conservation Laws," *SIAM Review*, Vol. 25, 1983, pp. 35–61.

[20]Harten, A., "High Resolution Schemes for Hyperbolic Conservation Laws," *Journal of Computational Physics*, Vol. 49, 1983, pp. 357–393.

[21]Yee, H. C., "Upwind and Symmetric Shock-Capturing Schemes," NASA TM 89464, May 1987.

[22]Sweby, P. K., "High Resolution Schemes Using Flux Limiters for Hyperbolic Conservation Laws," *SIAM Journal on Numerical Analysis*, Vol. 21, 1984, pp. 995–1011.

[23]van Leer, B., "Flux Vector Splitting for the Euler Equations," *Lecture Notes in Physics*, Vol. 170, 1982, pp. 507–512.
[24]Harten, A., "High Resolution Schemes for Hyperbolic Conservation Laws," *Journal of Computational Physics*, Vol. 49, 1983, pp. 357–393.
[25]Settles, G. S., Bogdonoff, S. M., and Fitzpatrick, T. J., "Detailed Study of Attached and Separated Compression Corner Flowfields in High Reynolds Number Supersonic Flow," *AIAA Journal*, Vol. 17, No. 6, 1979, pp. 579–585.
[26]Gerlinger, P., Stoll, P., and Brüggemann, D., "Multigrid Convergence Acceleration for Turbulent Supersonic and Hypersonic Flows," *Zeitschrift für Angewandte Mathematik und Mechanik*, Vol. 79, No. 3, 1999, pp. 681, 682.
[27]Bardina, J. E., Huang, P. G., and Coakley, T. J., "Turbulence Modeling Validation, Testing, and Development," NASA TM 110446, April 1997.
[28]Olejniczak, J., Wright, M. J., and Candler, G. V., "Numerical Study of Inviscid Shock Interactions on Double-Wedge Geometries," *Journal of Fluid Mechanics*, Vol. 352, 1997, pp. 1–25.
[29]Oertel, H., "Mach Wave Radiation of Hot Supersonic Jets Investigated by Means of the Shock Tube and New Optical Techniques," *Proceedings of the 12th International Symposium on Shock Tubes and Waves*, edited by A. Lifshitz and J. Rom, Magnus Press, Jerusalem, 1979, pp. 266–275.
[30]Tam, C. K. W., and Hu, F. H., "On the Three Families of Instability Waves of High-Speed Jets," *Journal of Fluid Mechanics*, Vol. 201, 1989, pp. 447–483.
[31]Kipke, K., and Hummel, D., "Untersuchungen an Längsangeströmten Eckenkonfigurationen im Hyperschallbereich, Teil I: Ecken Zwischen Ungepfeilten Keilen," *Zeitschrift für Flugwissenschaften*, Vol. 23, No. 12, 1975, pp. 417–429.
[32]D'Ambrosio, D., Marsilio, R., and Pandolfi, M., "Shock-Induced Separated Structures in Symmetric Corner Flows," AIAA Paper 95-2270, June 1995.
[33]van Keuk, J., and Ballmann, J., "Numerical Simulation of Symmetric Corner Flows in the Hypersonic Regime," *Notes on Numerical Fluid Mechanics*, No. 72, Vieweg Verlag, Wiesbaden, Germany, 1999, pp. 250–257.
[34]Coratekin, T. A., van Keuk, J., and Ballmann, J., "Preliminary Investigations in 2D and 3D Ramjet Inlet Design," AIAA Paper 99-2667, June 1999.
[35]Coleman, G. T., and Stollery, J. L., "Heat Transfer from Hypersonic Turbulent Flow at a Wedge Compression Corner," *Journal of Fluid Mechanics*, Vol. 56, 1972, pp. 741–752.
[36]Coakley, T. J., "Development of Turbulence Models for Aerodynamic Applications," AIAA Paper 97-2009, June 1997.
[37]Coratekin, T. A., Schubert, A., and Ballmann, J., "Assessment of Eddy Viscosity Models in 2D and 3D Shock/Boundary-Layer Interactions," *Engineering Turbulence Modelling an Experiments 4*, Elsevier, Munich, 1999, pp. 649–658.
[38]Kussoy, M. I., Horstman, K. C., and Horstman, C. C., "Hypersonic Crossing Shock-Wave/Turbulent-Boundary-Layer Interactions," *AIAA Journal*, Vol. 31, No. 12, 1993, pp. 2197–2203.
[39]Gaitonde, D., Shang, J., and Visbal, M., "Structure of a Double-Fin Turbulent Interaction at High Speed," *AIAA Journal*, Vol. 33, No. 2, 1995, pp. 193–200.
[40]Narayanswami, N., Horstman, C. C., and Knight, D. D., "Computation of Crossing Shock/Turbulent Boundary Layer Interaction at Mach 8.3," *AIAA Journal*, Vol. 31, No. 8, 1993, pp. 1369–1376.
[41]Spalart, P. R., "Trends in Turbulence Treatments," AIAA Paper 2000-2306, Sept. 2000.

H. M. Atassi
*Associate Editor*